

Flash sintering of rhenium at ambient temperature in < 1 minute with electrical current

Emmanuel A. Bamidele^a, Alan Weimer^c, and Rishi Raj^{a,b}

^aMaterials Science and Engineering Program, University of Colorado at Boulder, CO 80309, United States

^bDepartment of Mechanical Engineering, University of Colorado at Boulder, CO 80309-0427, United States

^c Department Chemical and Biological Engineering, University of Colorado Boulder, CO, 80309, United States

Submitted to: Journal of Refractory and Hard Materials

Corresponding Author; Rishi Raj, (303) 492-1029, rishi.raj@colorado.edu

Rishi Raj
University of Colorado Boulder
Boulder, CO 80309

rishi.raj@colorado.edu
(303) 492-1029

Key words: flash sintering, rhenium, current rate, electro-discharge sintering

Abstract

We show that rhenium can be sintered from powders to nearly full density (99.96%) by the direct injection of dc current (without a furnace) into dogbone shaped specimens in Ar atmosphere (< 100 ppm O₂). The current was increased at a rate of 1 A/s. The specimen sintered at a current density of 24 A mm⁻², when the specimen reached a temperature of 900°C. The following in-operando measurements are reported, (i) shrinkage strain with a rapid rate camera, (ii) resistivity measured by in-situ voltage and current, (iii) temperature measured with a pyrometer, and (iv) electroluminescence characterized with a spectrometer. The sintering cycle, during which the sample sintered to full density, was followed by two more flash cycles with dense specimens. In the first cycle the change in resistance exhibited a peak arising from the elimination of the high resistance of interparticle interfaces; the peak was absent in subsequent cycles. Plot of resistance with respect to temperature shows that resistivity of flashed rhenium is higher than literature values. The very rapid sintering and electroluminescence are attributed to the generation of defects in the form of vacancy-interstitial (Frenkel) pairs. The concentration of the Frenkels was estimated from in-situ calorimetry, where the difference between the electrical input energy and the enthalpy lost to radiation, convection and specific heat was attributed to the endothermic reaction for defect generation; dividing by enthalpy of formation of the defects yielded concentrations of up to 14 mol % of Frenkels.

1. Introduction

Flash sintering of ceramics was first reported in 2010¹, but its application to metals has remained unexplored. Various classes of ceramics, ranging from ionic conductors and semiconductors to ferroelectrics and insulators, have been processed using flash sintering approach².

Recent studies in our lab has shown that tungsten, a highly refractory metal, can be “flash sintered” within seconds at a temperature of 1000°C³. Unlike ceramics, which typically require furnace heating, metals can be sintered at ambient conditions. This is achieved by directly injecting current and increasing it continuously until the specimen sinters.

The flash sintering method of processing metals through current rate shares similarities with electro-discharge-sintering⁴. In the latter, a significant amount of energy is stored in a capacitor and rapidly discharged into a powder-pressed metal sample, causing it to sinter. The present current rate approach, however, offers better control: the duration of sintering can be varied from a few seconds to several minutes by adjusting the current rate. The flexibility allows for continuous, *in-operando* measurements of various parameters, including temperature, electroluminescence, and resistivity, offering a deeper understanding of the role of these parameters in the process.

Here we present current activated flash sintering of rhenium which melts at 3182 °C. Yet it sinters fully when activated with electrical current. A furnace is not necessary. As the current is increased the specimen heats up, and sinters quickly when the temperature reaches 900 °C, a remarkably low temperature for sintering a refractory metal. Full density, greater than 98% is achieved. It is postulated that current generates high concentration of defects that accelerate diffusion.

We report calorimetric measurements of the endothermic enthalpy during the flash process, which is ascribed to defect generation. It is obtained from the difference between the input electrical energy, relative to the energy lost to black body radiation (BBR), convection and specific heat. When divided by the enthalpy of formation of Frenkel defects we obtain their concentration to be equal to ~14 mol %, which is many orders of magnitude higher than the concentration expected from thermal equilibrium.

The results of current rate flash sintering of Re and other metals may have application in additive manufacturing. In conventional AM a part is built up digitally and then, separately, sintered.

With current rate flash sintering it may be possible to integrate current rate sintering with conventional AM, thereby parts that are end-user ready.

Flash sintering is a highly energy efficient process since energy is directly injected into the workpiece instead of using large furnaces that operate at very high temperatures for many hours where much of the heat is wasted. It is somewhat similar to the electrification of cars where energy goes directly to drive the wheels, sidestepping the inefficiencies of the internal combustion engine.

2. Method

Rhenium powders with a purity of 99.99% and a particle size of -325 mesh, were supplied by Fisher. About 1g of the powder, without binders, was pressed into a dogbone-shaped with hydraulic press from Dake Corporation, at a pressure of 140 MPa. The specimen measured 16 mm x 3.12 mm x 0.44 mm (gage length x width x thickness). Using the Archimedes method, we determined the green density, ρ_g to be ~74%.

The electrical current was supplied by Hewlett Packard 6261B power supply (0-20V, 0-50A). Tungsten electrodes, 1 mm in diameter, were attached through the 1.1 mm diameter holes located at the dogbone specimen ears. The current was injected at a constant rate of 1 A/s using a method adapted from Kumar et al.⁵ A home-built software was interfaced to the hardware via a National Instrument data acquisition device (NI DAQ). The voltage, the temperature and the current were recorded continuously as the current was increased at a constant rate.

The experiments were carried out at ambient temperature inside an argon-filled glovebox made by Vacuum Atmosphere Company, USA. The argon gas, 99.9% pure, was provided by Airgas, USA, maintaining at O₂ at 20 - 100 ppm.

The resistance was measured with a four point probe. The voltage probes were placed within the gage length of the dogbone at a distance of 6.9 mm. The voltage was measured with a Keithley digital multimeter. The resistance in Ω was determined from the voltage-to-current ratio. The resistivity, in units of Ω cm, was obtained by multiplying the resistance with the cross-sectional area and dividing by the distance between the voltage probes. The experiment's layout is depicted in Fig. 1.

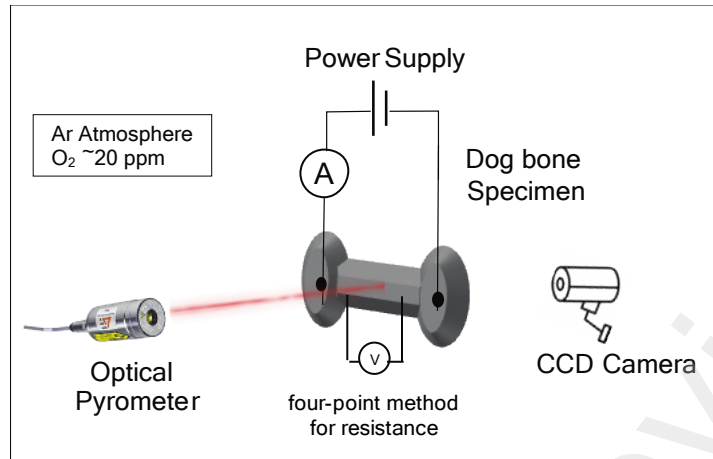


Fig. 1: Flash sintering of metals without a furnace

The rate of shrinkage of the specimen was obtained from pictures taken at the rate of 10 frames per second with a CCD camera from Imaging Source (Germany). The video was processed with Fiji software to determine the shrinkage. The temperature was measured with a CLTM-1HCF4-C3 pyrometer, manufactured by Micro-Epsilon (USA). This pyrometer operates within a temperature range of 250°C to 1200°C. Emissivity was configured at 0.3⁶, incorporating an error margin values shifting between 0.24 to 0.28 at elevated temperatures⁷.

3. Results

3.1 Sintering

The flash sintering experiment was conducted by increasing the current at a rate of 1 A/s. The corresponding shrinkage curve is presented in Fig. 2. The duration required for full sintering was 34 s. The sintered density can be calculated from the formula $\rho_g = \rho \exp (3\epsilon_1)$ ⁸. Here, ρ_g stands for the initial (green) density, ρ represents the time dependent density. ϵ_1 denotes the linear shrinkage strain. Therefore, with a shrinkage strain of 0.091 and an initial density of 74%, the resulting density > 97%; the Archimedes density was measured to be 99.6%.

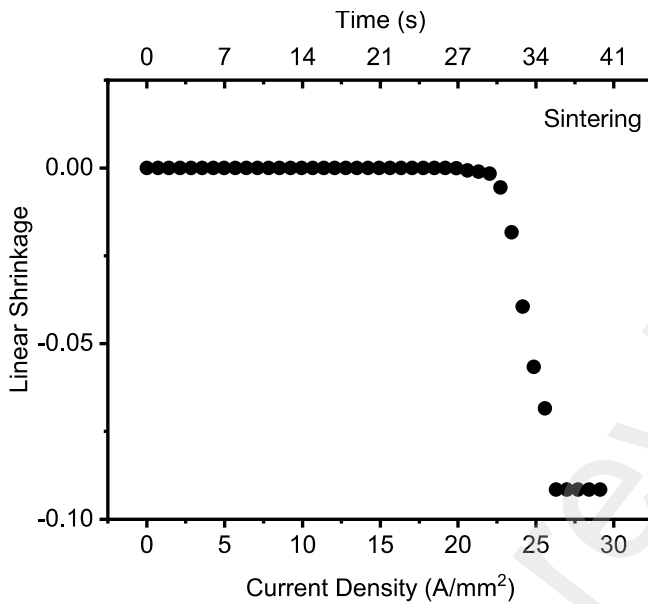


Fig. 2: Sintering strain as a function of the current density in the powder pressed dogbone sample.

3.2 Three Cycles

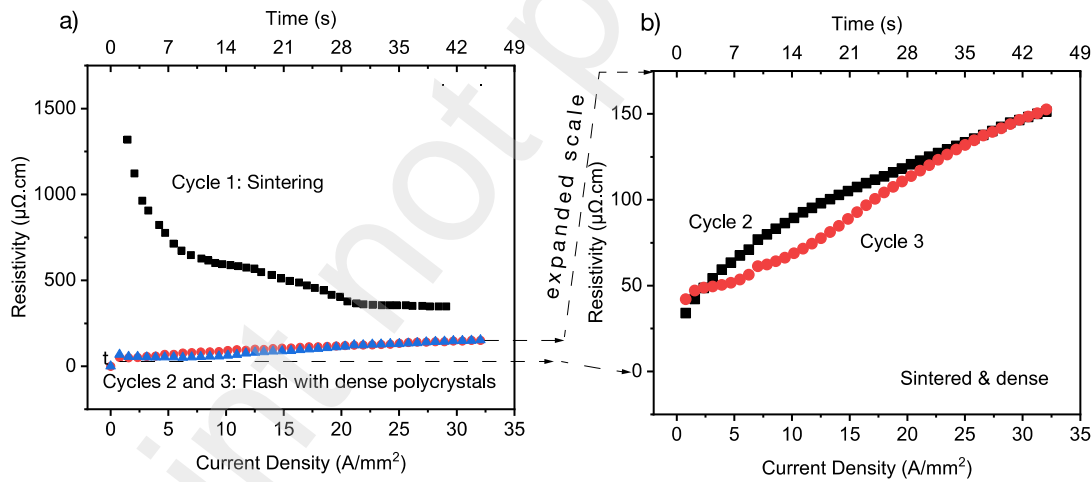


Figure 2: The change in resistance with current density. The first cycle refers to the sintering of the powder pressed sample. Cycles 2 and 3 were repeated on this sintered specimen. Sintering lowers the resistance and gives reproducible results. Note the expanded resistivity scale on the right.

The change in resistivity with current density is plotted in Fig. 3. The experiment was carried out with three cycles, with the same specimen. The first cycle represents sintering of the powder-pressed dog-bone specimen. After this cycle the specimen has sintered. The following two cycles

were carried out on this sintered specimen. Note that the transient peak in the resistance in the first cycle is absent in later cycles. It is attributed to the breakdown of the oxide-layer on the powder particles. A similar phenomenon was seen experiments with aluminum powders^{9.”} The continued reduction in resistance is ascribed to the sintering of pores.

3.3 Temperature and Luminescence

The change in temperature and the progression of electroluminescence with the current density, measured during cycle 2 are shown in Fig. 4. The temperature was measured with the pyrometer and the luminescence with the spectrometer (in the same experiment).

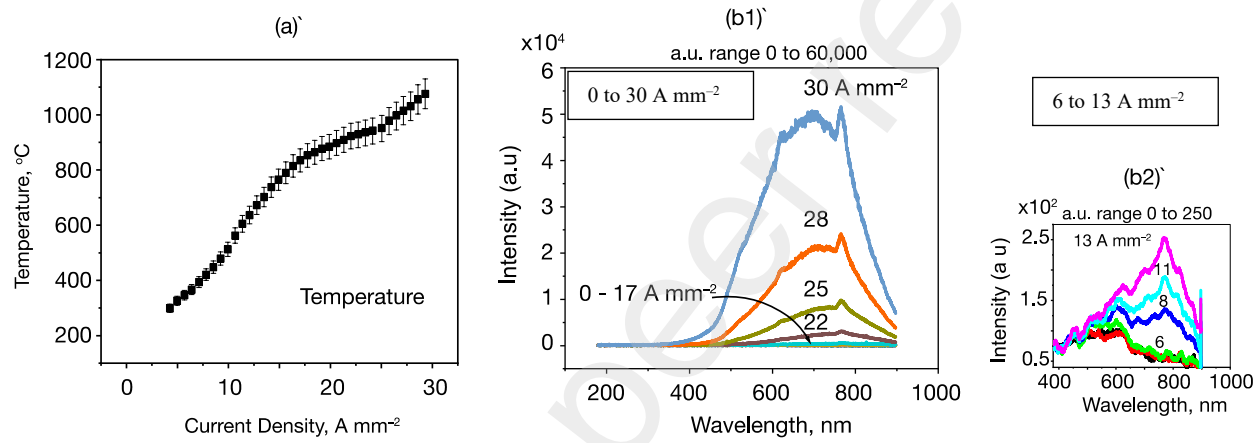


Fig. 4: The change in the specimen temperature with current density, (a) and with it the intensity of optical emission, (b). Figure (b) is shown with a wide range of intensity units at high current densities ($22 - 30 \text{ A mm}^{-2}$), and then with a high resolution scale which shows the emission at low current densities ($6 - 13 \text{ A mm}^{-2}$).

The optical emission is attributed to electroluminescence, as opposed to black body radiation, for a couple of reasons: (i) the temperatures measured are too low for optical emission from Joule heating, and (ii) the emission peak's intensity increases with rising specimen temperature but its position remains unchanged with respect to wavelength. In black body radiation the emission peak shifts towards shorter wavelengths as temperature rises.

3.4 The Resistivity

The in-operando resistance measured using the four-point technique, described in Section 2, is shown in Fig. 5. The measurement from cycle 2 is compared with the literature values which are represented in black color. Fig. 5¹⁰.

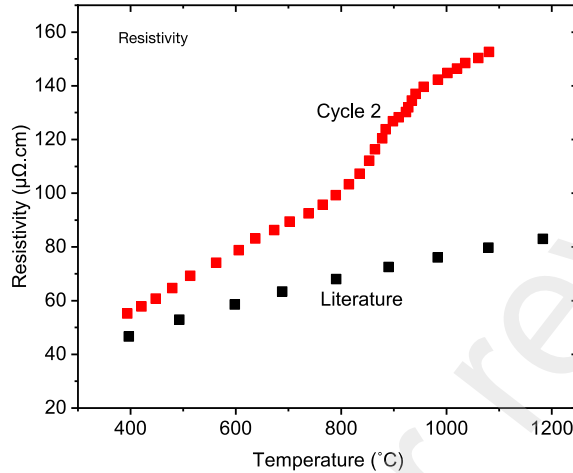


Fig. 5: Change in resistance with temperature in comparison to literature values. The resistance during flash is higher because of defects. The rate ¹¹of defect generation apparently accelerates at higher current densities.

The resistivity data from the flash experiment are higher than the data from the literature. This difference arises from defects that are generated during the flash experiment. The effect is stronger at higher temperature (higher current densities) which further supports this interpretation since current density has been found to be an important parameter in flash sintering¹¹. It also seems that the defects recombine, at least to a great extent, when the current is turned off; thus the starting resistance in Fig. 5 which represents the resistance at the end of Cycle 1 is low.

3.4 Calorimetry: Endothermic Enthalpy

A consistent observation in flash experiments is a deficit between the input electrical energy and the energy calculated from losses attributed to radiation, convection, and specific heat considerations. This disparity, known as the "energy deficit," provides a method for determining endothermic defect concentrations; obtained by dividing the energy deficit by the defect formation enthalpy¹².

The energy deficit, denoted as $\Delta H^*(t)$ in Joules, is given by the following expression:

$$\Delta H^*(t) = \int_0^t (W(t) - W^*(t)) dt \quad (1)$$

Where, $W(t)$ is the electrical energy (measured in Watts) expended in the specimen, and $W^*(t)$ is the sum of watts lost to radiation, convection, and specific heat. $W(t)$ is obtained from the product of the

current and the voltage. The losses attributed to radiation, convection, and specific heat are derived using the following expressions⁵:

$$W^*(t) = W_{BBR}^*(t) + W_{conv}^*(t) + W_{sph}^*(t) \quad (2)$$

$$W_{BBR}^*(t) = \epsilon_m S \sigma (T_K^4 - 298^4), \quad (3)$$

$$W_{conv}^*(t) = h S (T_K - 298), \quad (4)$$

$$W_{sph}^*(t) = m C_p \frac{dT_K}{dt} \quad (5)$$

Where the terms on the right-hand side of Eq. (2) refer to the energy lost to black body radiation, to convection and to specific heat. In Eq. (3), S is the specimen surface area, ϵ_m is the emissivity of Re (0.3), and σ is the Stefan-Boltzmann's constant ($5.6704 \times 10^{-8} \text{ W/m}^2\cdot\text{K}$); 298 K is the ambient temperature within the glove box. In Eq. (5) m is the specimen mass (0.00035 kg), and C_p , the specific heat, is equal to $137 \text{ J kg}^{-1} \text{ K}^{-1}$. T_K is the specimen temperature in Kelvin. Note that Eq. (2) is in units of Watts (J s^{-1}): it is integrated with respect to time to obtain the energy deficit in J.

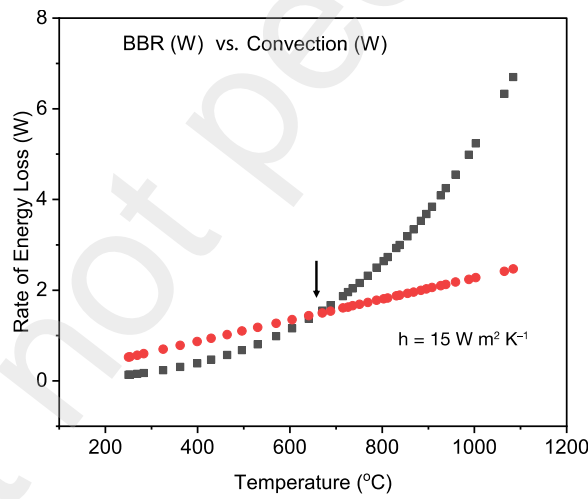


Fig. 6: The cross over from convection to black body radiation dominated loss at 600 °C which occurs for $h = 15 \text{ W m}^{-2} \text{ K}^{-1}$.

The convective heat transfer coefficient, h , in Eqn. (4) needs further attention. Its value in air ranges from 10 to 100 $\text{W m}^{-2} \text{ K}^{-1}$, contingent upon factors such as surface chemistry and morphology, gas velocity at the interface, and the heat capacity of the gas, which depends on pressure and the specific heat. Argon has a significantly lower heat capacity than nitrogen. Therefore, the heat transfer coefficient in Ar will be lower than in air.

Convection losses increase linearly with temperature while BBR losses scale with T^4 . This means convection is higher at lower temperatures but is overtaken by BBR at higher temperatures. The commonly accepted cross-over temperature, where energy loss transitions from convection to BBR, is approximately 600°C. This point is typically when the emitted light exhibits a faint red hue. A corresponding graph using our data is presented in Fig. 6, shows that the transition occurs near 600°C when $h = 15 \text{ W m}^{-2} \text{ K}^{-1}$.

In order to calculate the mole fraction of defects it is necessary to express ΔH^* in moles. We begin with calculating the moles of Re in the specimen; when divided by the molar volume of Re then gives the number of moles of Re in the specimen:

$$N_W = \frac{V_{\text{specimen}}}{V_{\text{molar}}} \quad (6)$$

The enthalpy in Eq. (3) may now be written in moles:

$$\Delta H_{\text{mol}}^* = \frac{\Delta H^*}{N_W} \quad (7)$$

To calculate the mole fraction of defects Eqn. (7) is divided by the formation energy of the defects in J mol^{-1} , which has been obtained from embedded atom potential in molecular dynamics simulation¹³. The mole fraction of defects is then given by

$$x_F = \frac{1}{E_F N_W} \frac{\Delta H^*}{\Delta H_{\text{mol}}^*} \quad (8)$$

Here, E_F is the formation energy of Frenkel defects in units of Joules mol^{-1} .

Substituting for $V_{\text{specimen}} = 22.5 \times 10^{-3} \text{ cm}^3$ and $V_{\text{molar}} = 8.67 \text{ cm}^3 \text{ mol}^{-1}$, and $E_F = 11.96 \text{ eV}$ into Eqns (6,7,8), after converting E_F from eV to J mol^{-1} (by multiplying by $96,500 \text{ J eV}^{-1}$).

Implementing the above procedures leads to the data given in Table I, in the following steps:

1. The input data is the temperature and electrical power input as a function of time.
2. The left-hand side of Eqn. (5 to 7) are obtained by inserting the temperature data into the right-hand side.
3. The watt measurements are converted to Joules through time integration.
4. Energy loss is calculated by combining BBR, convection and specific heat data.
5. The total energy loss is subtracted from the input energy to give ΔH^* .

6. Next Eqn. (8) gives the mole fraction of Frenkel defects. They are given in the right hand most column in Table I.

Time s	Pyrometer Temp K	Power Input Watts	BBR Watts	BBR Joule	Convec Watts	Convec Joules	Spec Joules	Total IN Joules	Total LOSS Joules	Deficit Joules	Frenkel
sec	°C		W	total J	W	total J	total J	J	J	kJ/mol	mol fraction
10	399	3.21	0.39	0.39	0.65	4.61	1.77	14.16	6.78	7.38	0.002
11	429	3.88	0.47	0.47	0.71	5.32	1.44	18.04	7.22	10.82	0.004
12	464	4.61	0.57	0.57	0.77	6.09	1.68	22.65	8.33	14.32	0.005
13	496	5.24	0.68	0.68	0.82	6.91	1.53	27.89	9.12	18.77	0.006
14	530	6.12	0.81	0.81	0.88	7.79	1.63	34.01	10.23	23.78	0.008
15	570	7.04	0.98	0.98	0.95	8.74	1.92	41.04	11.65	29.40	0.010
16	605	7.94	1.16	1.16	1.01	9.76	1.68	48.98	12.60	36.38	0.012
17	641	8.38	1.37	1.37	1.08	10.83	1.73	57.36	13.93	43.43	0.014
18	670	9.20	1.55	1.55	1.13	11.96	1.39	66.56	14.90	51.66	0.017
19	688	9.80	1.67	1.67	1.16	13.12	0.86	76.36	15.66	60.71	0.020
20	715	10.38	1.87	1.87	1.21	14.33	1.29	86.74	17.49	69.25	0.023
21	726	10.94	1.96	1.96	1.22	15.55	0.53	97.68	18.04	79.65	0.027
22	736	11.86	2.04	2.04	1.24	16.79	0.48	109.54	19.31	90.23	0.030
23	751	12.58	2.16	2.16	1.27	18.06	0.72	122.12	20.94	101.18	0.034
24	769	13.15	2.32	2.32	1.30	19.36	0.86	135.27	22.54	112.73	0.038
25	788	14.08	2.50	2.50	1.33	20.69	0.91	149.35	24.10	125.25	0.042
26	803	14.90	2.64	2.64	1.36	22.05	0.72	164.25	25.41	138.84	0.046
27	812	15.44	2.73	2.73	1.38	23.43	0.43	179.69	26.59	153.10	0.051
28	831	15.01	2.93	2.93	1.41	24.84	0.91	194.70	28.68	166.02	0.055
29	838	15.72	3.00	3.00	1.42	26.26	0.34	210.42	29.60	180.82	0.060
30	855	16.41	3.19	3.19	1.45	27.71	0.82	226.83	31.71	195.11	0.065
31	868	17.05	3.34	3.34	1.47	29.18	0.62	243.88	33.15	210.73	0.070
32	884	17.92	3.53	3.53	1.50	30.68	0.77	261.80	34.98	226.81	0.076
33	896	18.81	3.68	3.68	1.52	32.20	0.58	280.61	36.46	244.15	0.081
34	908	19.72	3.84	3.84	1.54	33.75	0.58	300.33	38.16	262.17	0.087
35	927	22.05	4.09	4.09	1.58	35.32	0.91	322.38	40.33	282.05	0.094
36	938	24.48	4.25	4.25	1.60	36.92	0.53	346.86	41.69	305.17	0.102
37	959	26.27	4.55	4.55	1.63	38.55	1.01	373.13	44.10	329.02	0.110
38	988	26.22	4.99	4.99	1.68	40.23	1.39	399.35	46.62	352.73	0.118
39	1003	26.52	5.24	5.24	1.71	41.94	0.72	425.87	47.90	377.97	0.126
40	1065	28.00	6.33	6.33	1.82	43.76	2.97	453.87	53.06	400.80	0.134
41	1084	29.93	6.70	6.70	1.85	45.61	0.91	483.80	53.22	430.58	0.144

Table I: Frenkel Defect Analysis Based on Energy Deficit

Plots for the energy deficit in kJ mol^{-1} , and the mole fraction of Frenkel pairs are plotted in Fig. 7 (a)&(b). The defect concentration rises to 14% mole fraction. Comparatively, values calculated from thermal equilibrium are many, many orders of magnitude lower. Comparable experiments with nickel and tungsten gave values of 3% for nickel, and 26% for tungsten.

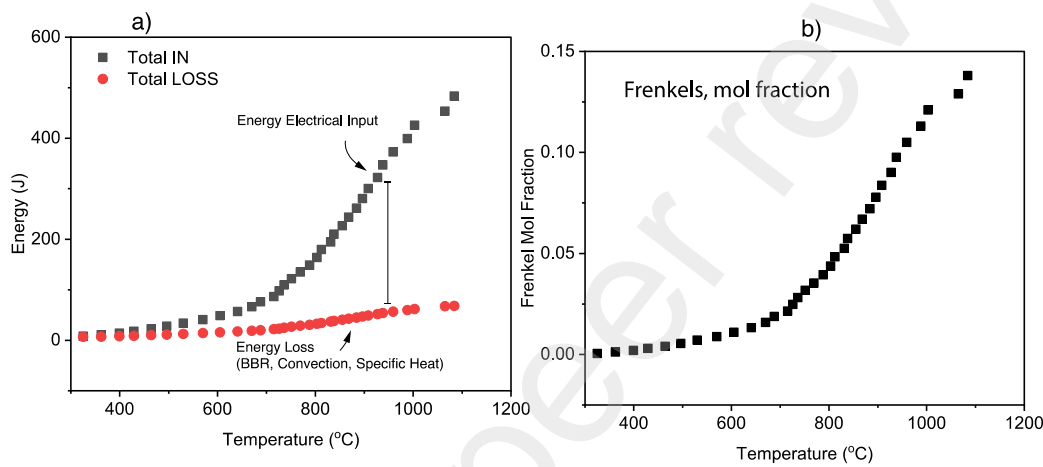


Fig. 7: (a) Plots of the energy deficit as given by Eqs (1) to (5). . The energy input is greater than the energy dissipation indicating an endothermic reaction, which is ascribed to defect (Frenkels) generation (b).3.5 Phenomenological Description of Flash in Metals

The pattern of flash sintering observed in the present study is similar to tungsten (in review). A common observation is that resistance is higher than the literature values, pointing to the role of defects. The three regimes of behavior in current rate flash sintering of metals are shown in Fig. 8. The pattern starts with an incubation time, followed by the onset of electroluminescence, and finally by sintering. Similar behavior was observed in W and Ni.

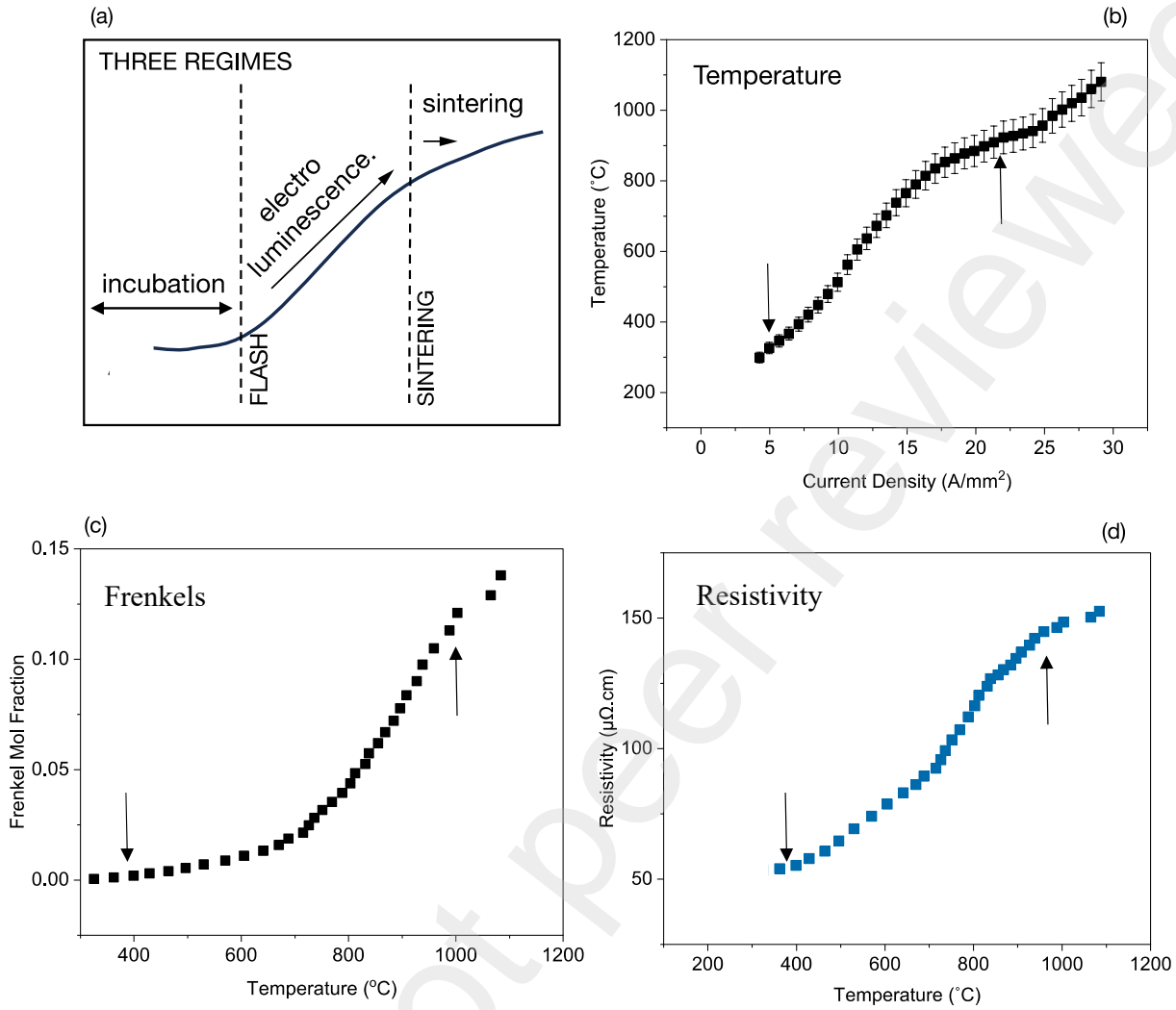


Fig. 8: Phenomenological behavior of flash in metals showing the onset of flash, sintering, temperature and resistivity with increasing current density. The temperature is plotted with respect to current density, and the defects and resistivity with respect to temperature.

4. Discussion

This is the second report on flash sintering of a refractory metal following the work on tungsten. Both are refractory metals with melting points of 3182°C for Re and 3383°C for W. Solid state diffusion theories link the diffusion coefficient to the melting point of the metal¹⁴. Generally sintering occurs at 0.75T_M, over a period of several hours. In comparison the current rate flash sintering occurs near 1000 °C in about one minute. Both metals sintered at a current density of 20 – 24 A mm⁻² (for similar workpiece geometry). Apparently solid-state diffusion in flash is ultrafast.

Diffusion coefficients are products of defect concentration and the mobility of atoms. The high diffusivity may be attributed to the concentration of defects described in the Section 3.4. Indeed, real-time measurements of diffusion coefficients across bilayers in ceramics suggest that diffusion rates in flash are almost 10^8 times faster¹⁵. The activation energy for diffusion are found to be one half to a third of the values in literature¹⁶.

Recently the superposition of magnetic fields have been shown to drive the flash into a standalone workpieces without electrical contacts. It is likely that flash is a solid-state plasma¹⁷ which responds to magnetic fields.

It is becoming increasingly evident that flash sintering has broad implications. For instance, rhenium, nickel and tungsten, despite considerably different melting points, show similar behavior for example the onset of luminescence at $5\text{-}7 \text{ A mm}^{-2}$, reaching full sintering between $20\text{-}24 \text{ A mm}^{-2}$ (in specimens of similar geometry).

5. Summary

Flash sintering of rhenium powders is a new paradigm for densification of refractory metals. The development has significance in additive manufacturing of metals, paving the way for in-situ densification where AM is integrated with current rate flash sintering.

The flash “ecosystem” has additional novel properties. Flash has been shown to produce far from equilibrium phases; that is, phases that do not fit classical thermodynamic behavior¹⁸. Such findings hold the possibility of new solid-state electrolytes for Li⁺ batteries, with high ionic conductivities¹⁹.

6. Acknowledgements

This work was supported by a grant from NASA, ESI Program under the grant number 80NSSC21K0225. Lively discussions with Dr. Jhonathan Rosales, and his encouragement as the work progresses is gratefully acknowledged. We are grateful to Davis Conklin from Alan Weimer Lab for providing the rhenium powders used in this study.

References

1. Cologna, M., Rashkova, B. & Raj, R. Flash sintering of nanograin zirconia in< 5 s at 850 C. *J. Am. Ceram. Soc.* **93**, 3556–3559 (2010).
2. Raj, R. Analysis of the Power Density at the Onset of Flash Sintering. *J. Am. Ceram. Soc.* **99**, 3226–3232 (2016).
3. Bamidele, Emmanuel, Raj, Rishi, & Jalali, I. A. Syed. Flash sintering of tungsten in a few seconds at 1400 oC. (2023).
4. Yurlova, M. S. *et al.* Electric pulse consolidation: an alternative to spark plasma sintering. *J. Mater. Sci.* **49**, 952–985 (2014).
5. Kumar MK, P., Yadav, D., Lebrun, J. & Raj, R. Flash sintering with current rate: A different approach. *J. Am. Ceram. Soc.* **102**, 823–835 (2019).
6. Köster, U. *et al.* In-pile arrangements of reactor-based RIB facilites. *Nucl. Instrum. Methods Phys. Res. Sect. B Beam Interact. Mater. At.* **126**, 253–257 (1997).
7. McClure, J., Boboridis, K. & Cezairliyan, A. Radiance temperatures (in the wavelength range 521 to 1500 nm) of rhenium and iridium at their melting points by a pulse-heating technique. *Int. J. Thermophys.* **20**, 1137–1148 (1999).
8. Separation of Cavitation-Strain and Creep-Strain During Deformation - Raj - 1982 - Journal of the American Ceramic Society - Wiley Online Library.
<https://ceramics.onlinelibrary.wiley.com/doi/abs/10.1111/j.1151-2916.1982.tb10397.x>.
9. McWilliams, B., Yu, J., Kellogg, F. & Kilczewski, S. Enhanced Sintering Kinetics in Aluminum Alloy Powder Consolidated Using DC Electric Fields. *Metall. Mater. Trans. A* **48**, 919–929 (2017).
10. Bryskin, B. D. Evaluation of properties and special features for high-temperature applications of rhenium. in vol. 246 278–291 (American Institute of Physics, 1992).
11. Francis, J. S. C. & Raj, R. Influence of the Field and the Current Limit on Flash Sintering at Isothermal Furnace Temperatures. *J. Am. Ceram. Soc.* **96**, 2754–2758 (2013).
12. Mishra, T. P., Neto, R. R. I., Raj, R., Guillon, O. & Bram, M. Current-rate flash sintering of gadolinium doped ceria: Microstructure and Defect generation. *Acta Mater.* **189**, 145–153 (2020).
13. Bonny, G., Bakaev, A., Terentyev, D. & Mastrikov, Y. A. Interatomic potential to study plastic deformation in tungsten-rhenium alloys. *J. Appl. Phys.* **121**, (2017).
14. Shewmon, P. G. *Diffusion in Solids*. (McGraw-Hill, 1963).
15. Jalali, S. I. A. & Raj, R. Reactive flash sintering in a bilayer of zirconia and lanthana: Measurement of the diffusion coefficient in real time. *J. Am. Ceram. Soc.* **n/a**,
16. Motomura, H., Tamao, D., Nambu, K., Masuda, H. & Yoshida, H. Athermal effect of flash event on high-temperature plastic deformation in Y₂O₃-stabilized tetragonal ZrO₂ polycrystal. *J. Eur. Ceram. Soc.* **42**, 5045–5052 (2022).
17. Jalali, S. I. A. & Raj, R. Touch-free flash sintering with magnetic induction within a reactor activated by the usual flash method. *J. Am. Ceram. Soc.* **n/a**, 2022;1–6 (2022).
18. Lebrun, J.-M. *et al.* Emergence and extinction of a new phase during on-off experiments related to flash sintering of 3YSZ. *J. Am. Ceram. Soc.* **98**, 1493–1497 (2015).
19. Clemenceau, T. & Raj, R. Higher conductivity of non-stoichiometric lithium lanthanum zirconate ceramics made by reactive flash synthesis. *MRS Commun.* (2022)
doi:10.1557/s43579-022-00162-z.

Preprint not peer reviewed

List of Figures

Fig. 1: : Flash sintering of metals without a furnace.

Fig. 2: Sintering strain as a function of the current density in the powder pressed dogbone sample.

Fig. 3 (a) The change in resistance with current density in the pristine powder pressed sample (cycle 1), and then with the same cycle with repeated flash, but this time on a dense sample, marked as cycles 2 and 3. Note the much higher resistivity scale used for cycles 2 and 3 in Fig. 3(b).

Fig. 4: The change in the specimen temperature with current density, (a) and with it the intensity of optical emission, (b). Figure (b) is shown with a wide range of intensity units at high current densities ($22 - 30 \text{ A mm}^{-2}$), and then with a high resolution scale which shows the emission at low current densities ($6 - 13 \text{ A mm}^{-2}$).

Fig. 5: Change in resistance with temperature in comparison to literature values. The resistance during flash is higher because of defects. The rate of defect generation apparently accelerates at higher current densities.

Fig. 6: The cross over from convection to black body radiation dominated loss at $600 \text{ }^{\circ}\text{C}$ which occurs for $h = 15 \text{ W m}^{-2} \text{ K}^{-1}$.

Fig. 7: (a) Plots of the energy deficit as given by Eqs (1) to (5). . The energy input is greater than the energy dissipation indicating an endothermic reaction, which is ascribed to defect (Frenkels) generation (b).

Fig. 8: Phenomenological behavior of flash in metals showing the onset of flash, sintering, temperature and resistivity with increasing current density. The temperature is plotted with respect to current density, and the defects and resistivity with respect to temperature.